International Journal of Thermal Sciences 179 (2022) 107707

Contents lists available at ScienceDirect

International Journal of Thermal Sciences

journal homepage: www.elsevier.com/locate/ijts

Effect of volume ratio on thermocapillary convection in annular liquid pools in space

Jia Wang [a,1], Ziyi Guo [a,b,1], Chengjun Jing [c], Li Duan [a,b], Kai Li [a,b,*], Wenrui Hu [a,b]

[a] Key Laboratory of Microgravity, Institute of Mechanics, Chinese Academy of Sciences, Beijing, 100190, China
[b] School of Engineering Science, University of Chinese Academy of Sciences, Beijing, 100149, China
[c] College of Architecture and Environment, Sichuan University, Chengdu, 610064, China

ARTICLE INFO

Keywords:
Thermocapillary convection
Microgravity
Transition
Annular pool
Numerical analysis

ABSTRACT

In systems with liquid/liquid or liquid/gas interface under microgravity, and even in shallow liquid layers in the terrestrial conditions, thermocapillary force takes the principal role to drive natural convections. A series of numerical simulations are conducted to investigate the stability limit of axisymmetric steady thermocapillary flow in annular liquid pools with curved and adiabatic liquid surface for eight volume ratios $0.809 \leq Vr \leq 1.173$, where Vr is defined as (liquid vol/vol of the annular gap). Simulations provide the critical temperature difference ΔT_c, frequency f_c, and azimuthal wave number m_c for each liquid pool. At the critical condition, oscillations start in form of standing wave. At the slightly supercritical condition (ΔT^*), the standing waves turn to traveling oscillations. The calculated ΔT_c values decrease with the increase of Vr. A simulation code with a convective thermal boundary condition in the liquid surface suggests that heat transfer through the liquid surface significantly increases the ΔT_c value.

1. Introduction

In systems with liquid/liquid or liquid/gas interface under microgravity, and in shallow liquid layers even under terrestrial conditions, thermocapillary convection (TC) occurs when temperature or concentration gradient arises along the interface. With remarkable progress in space activities, TC has been one of the fundamental subjects in microgravity fluid physics and space fluid/heat management [1–3]. Annular liquid pool is a typical model for investigations of the thermocapillary convection. In this configuration, the basic TC is axisymmetric stationary when the temperature difference (ΔT) applied between the inner and outer walls is small. When ΔT exceeds a certain threshold value, i.e. the critical temperature difference ΔT_c, the basic flow becomes unstable against three-dimensional oscillating disturbances and turns into oscillatory flow in form of hydrothermal waves (HTW) propagating in the azimuthal direction. With further increased ΔT, the oscillatory TC exhibits complex flow patterns and spatio-temporal evolutions depending on the control parameters such as the Reynolds number (Re), the Prandtl number (Pr) and the pool dimensions [4–6].

Ostrach et al. [7] carried out the first space experiment on the steady flow and temperature distributions in circular and annular liquid pools in 1992. Their pool was composed of a cooled outer wall (diameter 10 cm) and a heated center rod (diameter 1 cm), and the liquid depth was 5 cm. In another space flight, Ostrach et al. [8] measured the temperature distribution and determined the critical conditions for the onset of oscillatory flow in small liquid pools with different sizes. Thereafter, space experiments on the stability of TC in annular pools have been conducted with a deep pool heated at the inner wall [9,10] and a shallow pool heated at the outer wall [11–14]. Recently, Kang et al. [15–17] conducted a series of space experiments using an annular liquid pool on board the China's SJ-10 recovery satellite. They investigated the effects of the free-surface shape on the stability of TC. Dynamics and transitions of the wave pattern were observed and the nonlinear dynamics of the traveling waves, standing waves, and counter-propagating waves were also studied.

In addition to the rare and valuable space experiments, many theoretical and numerical studies have been reported. Based on the linear stability analysis (LSA), Smith and Davis [18,19] first predicted that TC in an infinite liquid layer driven by the imposed temperature gradient parallel to the free surface in zero gravity would become unstable against three dimensional disturbances. They found stationary

* Corresponding author. National Microgravity Laboratory, Institute of Mechanics, Chinese Academy of Sciences, Beijing, 100190, China.
E-mail address: likai@imech.ac.cn (K. Li).
[1] First Authors.

https://doi.org/10.1016/j.ijthermalsci.2022.107707
Received 6 March 2022; Received in revised form 27 April 2022; Accepted 19 May 2022
Available online 26 May 2022
1290-0729/

longitudinal rolls and unsteady hydrothermal wave (HTW) in the case of a flat free surface. Smith [20] also explained the mechanism of the hydrothermal wave instability. Pukhnachev [21,22] built theoretical models of flows concerning thermocapillary forces and free surface deformation, which contributes to fundamental hydrodynamic theories in this field. Shvarts and Boudlal [23] theoretically studied advective flow in a horizontal rotating liquid film of infinite extent with free surface. Then Knutova and Shvarts [24] conducted further investigations on an advective thermocapillary flow in a weakly rotating horizontal liquid layer in microgravity conditions with linear stability analysis. Sim and Zebib [25] numerically investigated the effects of the Coriolis force and heat loss/gain through the liquid surface on the critical conditions for the onset of oscillatory thermocapillary convection (HTW) in an open annulus heated from the inner wall. Their results showed that heat loss from the free surface would stabilize the basic steady flow(i.e., increases the critical Reynolds number). Sim et al. [26] also numerically investigated the effect of the aspect ratio of the pool and heat exchange between the liquid surface and the ambient environment on the critical condition for the onset of HTW in annular pools heated from the outer wall. Their results showed that heat loss through the interface increased Re_c and decreased critical frequency. Wu et al. [27] numerically studied the characteristics of thermo-soluto-capillary flow bifurcations and pattern evolutions of binary fluid in a rotating cylinder partially covered by a rotating circular disk attached to the liquid surface (like the Czochralsky crystal growth furnace). They observed various flow patterns at different temperature differences and disk/pool rotation rates. Bessonov and Polezhaev [28–30] numerically investigated the convection and heat transfer in the Czochralski model. Bekezhanova and Goncharova [31–34] theoretically and numerically studied thermocapillary flows considering evaporation, and their works provide deeper understandings about thermocapillary flow with the phase transition. Shi et al. [35] determined the critical conditions for the onset of oscillatory flows in a shallow annular pool of silicone oil (Pr = 6.7). Hoyas et al. [36] obtained the stability diagram for the flow in annular pools of silicone oil heated at the inner wall by LSA.

Note that most of these studies assumed planar free surface. However, under microgravity, the planar free-surface assumption is not always valid and non-flat liquid surface shape causes diversities of the spatio-temporal evolutions of HTW and changes the critical conditions. Therefore, the volume ratio of the liquid zone ($Vr = V_l/\pi h\ (r_0^2 - r_i^2)$), which denotes the ratio of the liquid volume (V_l) to the volume of the annular gap between the walls, is one of the important factors for the stability of the basic flow especially under microgravity [3]. This paper reports the results of 3D direct numerical simulations (DNS) for the thermocapillary flow in annular liquid pools under various temperature differences ΔT between the inner and outer walls. Simulations reveal that the flow and temperature fields under small ΔT is axisymmetric, this flow is named as the "basic flow". At a certain ΔT (the critical temperature difference ΔT_c) the basic flow changes to a three-dimensional oscillatory flow with a wave number m_c and a frequency f_c. At the critical stage ($\Delta T = \Delta T_c$), the temperature and velocity fields oscillate in form of standing waves, i.e. apparently without any drifts in the azimuthal direction. At and over the slightly supercritical stage ($\Delta T = \Delta T^*$) the oscillations appear as traveling waves. Although the numerical results predict critical temperature differences smaller than the experimental results, both show similar decreasing trends of critical temperature and frequencies as volume ratios increase. To explain the discrepancy, numerical simulations which consider heat exchange between the liquid surface and ambient gas at 391 K using a convective thermal boundary condition on the liquid surface are also conducted. The results for $Vr = 1.0$ show that the heat exchange stabilizes the basic flow (i.e. increases ΔT_c value), which can account for the lower critical value obtained by the numerical simulations.

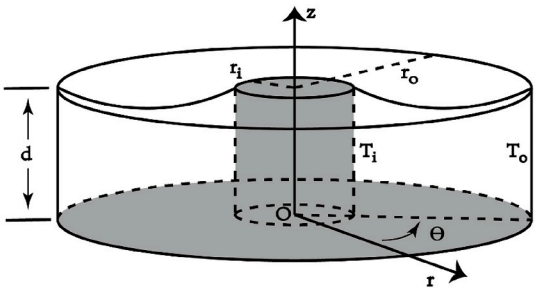

Fig. 1. Sketch of annular pool identical to SJ-10 space experiments.

Table 1
Variable Φ, dimensionless parameter R_Φ, source term S_Φ and S_Φ* in Eq. (1).

Variable	Φ	R_Φ	S_Φ	S^*_Φ
Mass	1	∞	0	0
Momentum (jth comp.)	U_j	1	$-\frac{\partial P}{\partial X_j}$	$-\frac{\partial P}{\partial \xi_k}\frac{\partial \xi_k}{\partial X_j}$
Energy	Θ	$_{Pr}$	0	0

2. Model and methodology

2.1. Model

Fig. 1 shows a top-opened annular liquid pool which is identical to the space experiment apparatus on board China's SJ-10 recovery satellite [15–17]. The radius of the central column is $r_i = 4$ mm, radius of the outer wall is $r_o = 20$ mm, and the gap width is $\Delta r = r_o$-r_i. The heights of the central column and outer wall are both $d = 12$ mm. The central column is heated (T_i), and the outer wall is fixed at 290 K (T_o). The working fluid is 2 cSt silicone oil with $Pr = 28.01$.

The mathematical model is composed of the continuity, momentum and energy equations for the fluid. The dimensionless governing equations can be written as

$$\left(\frac{\partial \Phi}{\partial \tau} + \frac{\partial U_i \Phi}{\partial X_i}\right) - \frac{1}{R_\Phi}\frac{\partial}{\partial X_i}\left(\frac{\partial \Phi}{\partial X_i}\right) = S_\Phi \tag{1}$$

where Φ is a general transport variable, X_i the i-th Cartesian coordinate, U_i the i-th Cartesian velocity component, τ the time, S_Φ the source of Φ, and R_Φ a dimensionless parameter. In deriving the above equations, the non-dimensional length, velocity, temperature with respect to To, pressure and time are scaled by the reference length, velocity, temperature, pressure and time, which are chosen respectively as

$$l_{ref} = d,\ \ u_{ref} = \frac{\nu}{d},\ \ T_{ref} = T_i - T_o,\ \ p_{ref} = \rho u_{ref}^2,\ \ \tau = \frac{l_{ref}}{u_{ref}},$$

where p is the pressure, T the fluid temperature, ρ the density, ν the kinematic viscosity, α the thermal diffusivity and $Pr = \nu/\alpha$. Table 1 shows the definition of Φ, S_Φ and R_Φ for each equation.

2.2. Methodology

According to the advantages discussed in Ref. [37], a block-structured grid [38] with matching/non-overlapping interfaces was adopted in the present study. The domain was divided into finite control volumes (CVs). Non-uniform grid assignment is adopted in the physical domain to increase the resolution near the boundaries.

Due to the non-orthogonality of the grids and the curvilinear boundaries, the boundary-fitted-coordinate (BFC) method [39] is adopted. The governing equation (Eq. (1)) in the physical space (X_i, i = 1,2,3) is first transformed to the computational space (ξ_i, i = 1,2,3) and takes the following form after the coordinate transformation [40]:

$$\left(\frac{\partial \Phi}{\partial \tau}+\frac{1}{J}\frac{\partial U_k^* \Phi}{\partial \xi_k}\right)-\frac{1}{R_\Phi}\frac{1}{J}\frac{\partial}{\partial \xi_k}\left(Jg_{kl}\frac{\partial \Phi}{\partial \xi_l}\right)=S_\Phi^* \tag{2}$$

where $J = \partial(X_1,X_2,X_3)/\partial(\xi_1,\xi_2,\xi_3)$ is the Jacobian matrix, and $g_{kl}=(\partial\xi_k/\partial X_i)(\partial\xi_1/\partial X_i)$ is the metric tensor. In Eq. (2), U_k^* is the contravariant velocity, which is defined as $U_k^*=(JU_j\,\partial\xi_k)/(\partial X_j)$, S_Φ^* is the source term after the coordinate transformation given in Table 1.

The shape function is adopted to estimate the derivatives related to the coordinate transformation $\partial X_i/\partial\xi_j$, where X_i is expressed as $X_i = \sum_{n=1}^{8}\Phi_n(\xi_1,\xi_2,\xi_3)X_{ic}$, $i = 1, 2, 3$, Φ_n (ξ_1, ξ_2, ξ_3) is the shape function and subscript c denotes the corner points of the CV. This method is found to be able to improve the accuracy of the metric valuables such as the Jacobian matrix and the metric tensor.

Eq. (2) is discretized using a fully conservative finite-volume method with a non-staggered arrangement of the variables [41]. Central difference is used for all spatial derivatives and first order forward difference for the time derivatives. For the convective term, QUICK scheme [42] is applied. Based on the continuity equation, a pressure-correction equation is derived according to SIMPLE algorithm [43]. To ensure the correct coupling of pressure and velocity fields, the well-known momentum interpolation technique of Rhie and Chow [41] is applied. The time interval $\Delta\tau = 10^{-5}$ is tested to be suitable.

2.3. Boundary conditions and initial conditions

With the curvilinear free surface, the non-dimensional boundary conditions can be written as follow:

1) B.C. at the free surface

$$\vec{t}_{\xi_1}\cdot\prod\vec{n}=Ma\nabla\Theta\cdot\vec{t}_{\xi_1},\ \vec{t}_{\xi_2}\cdot\prod\vec{n}=Ma\nabla\Theta\cdot\vec{t}_{\xi_2},\vec{U}\cdot\vec{n}=0,\nabla\Theta\cdot\vec{n}=0 \tag{3}$$

where $\vec{t}$ and $\vec{n}$ are the tangential and normal unit vectors of the free surface, respectively, Π is the stress tensor and $\vec{U}$ is the velocity vector. Subscripts ξ_1, ξ_2 denote the curvilinear coordinates. In our coordinate assignment, for the region below the free surface, ξ_1 corresponds to the radial direction along the free surface and ξ_2 is the circumferential direction. Ma is the Marangoni number defined as $Ma = -(\gamma_T\,\Delta Td)/\mu\nu$.

2) B.C. at the central column and outer wall:

$$\vec{U}=0,\quad \Theta_i=1,\quad \Theta_o=0 \tag{4}$$

3) B.C. at the bottom:

$$\vec{U}=0,\nabla\Theta\cdot\vec{n}=0 \tag{5}$$

Details of the treatment of the boundary conditions at free surface are described in Ref. [44].

The fluid is assumed motionless initially, and the temperature difference is assumed directly applied between the central column and outer wall at the beginning of the calculation $\tau = 0$. On the other hand, the free surface shape is calculated based on the Young-Laplace equation at $\tau = 0$ and it remains unchanged in the subsequent calculations of the velocity and thermal fields.

2.4. Verification of the model

The validity of the treatment of boundary conditions at the curvilinear surface proposed above was described in Ref. [44] in detail. Moreover, three grid numbers (173635, 332145, 637065), which corresponds to ($41 \times 121 \times 35$), ($61 \times 121 \times 45$) and ($81 \times 121 \times 65$) in (r, θ,z) directions, are used to carry out the grid independence test. For the planar free surface case, the determined ΔT_c is 9.10 K, 8.33 K and 8.16 K respectively. The corresponding relative difference decreases from 12% to 2%. Therefore, the grid number 332145 is adopted in the subsequent calculations in consideration of both calculation accuracy and computation cost.

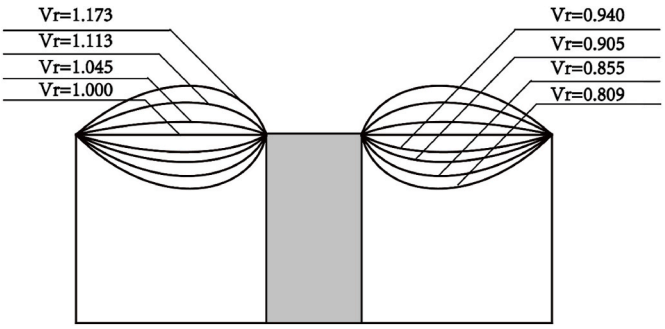

Fig. 2. Free-surface morphologies for liquid pools with various liquid volume-ratios.

3. Results and discussion

3.1. Liquid surface configurations and axisymmetric steady flow

In the present study, instabilities of thermocapillary flow in annular liquid pools with different liquid volume-ratios (Vr = 0.809, 0.855, 0.905, 0.940, 1.000, 1.045, 1.113 and 1.173) are investigated. Hereafter, ΔT [K] and f [1/sec] instead of the non-dimensional parameters Ma and the non-dimensional frequency are used. Since the triple-phase lines are assumed to anchor at the upper edges of the annular gap, the free-surface shape changes from concave to convex as Vr increases, as shown in Fig. 2. The basic flow is axisymmetric and steady before the onset of oscillations. Fig. 3 shows the temperature distribution in liquid pools with different volume ratios right before the onset of the oscillatory flow. Highly distorted isotherms suggest that the basic flow is very strong and creates thermal boundary layers along borh the inner and outer walls.

3.2. Critical conditions for the onset of oscillatory TC

When ΔT exceeds the critical value ΔT_c, the basic flow becomes unstable and oscillatory TC sets on in the form of hydrothermal-waves of m_c (wave number) and f_c (frequency). Spatio-Temporal Diagram (STD) of surface temperature along the azimuthal direction at r = 12 mm for $Vr = 0.809$ are shown in Fig. 5 to present the thermal patterns. Fig. 5a is the STD at the critical stage (ΔT_c = 12.95 K) and Fig. 4b at the slightly supercritical stage (ΔT^* = 13.40 K). The checkerboard pattern of Fig. 4a indicates a standing oscillation caused by interactions between two hydrothermal waves with $m = 4$ traveling in the opposite azimuthal directions. On the other hand, Fig. 5b, the STD at the slightly supercritical stage, is composed of 4 white and 4 black slanted parallel lines, indicates a traveling HTW of $m = 4$.

The critical conditions (ΔT_c, m_c and f_c) and slightly supercritical condition (ΔT *, m* and f *) for the eight Vr values are tabulated in Table 2. The DNS results show that ΔT_c decreases with increasing Vr. Number of azimuthal waves (m) of the DNS results are all $m = 4$ except for $m = 3$ in the case for $Vr = 1.173$. These results imply that there is a switch of instability mode for $Vr = 1.173$, and the switch leads to the increase of the critical frequency f_c between cases for $Vr = 1.113$ and 1.173, which is similar to the linear stability results for $Pr = 0.011$ obtained by Liu et al. [45].

3.3. Standing oscillatory flows

The 3D structure of the instantaneous temperature field of the

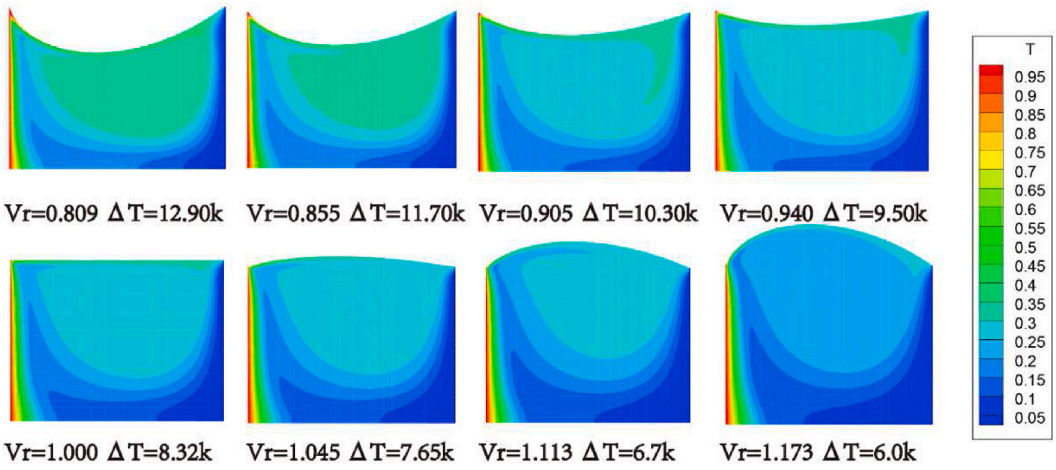

Fig. 3. Isotherms of the axisymmetric steady TC in liquid pools of different volume-ratios. (on a vertical cut at $\varphi = 0$ and at temperature difference $\Delta T = \Delta T_c$ – (0.02–0.05 K)).

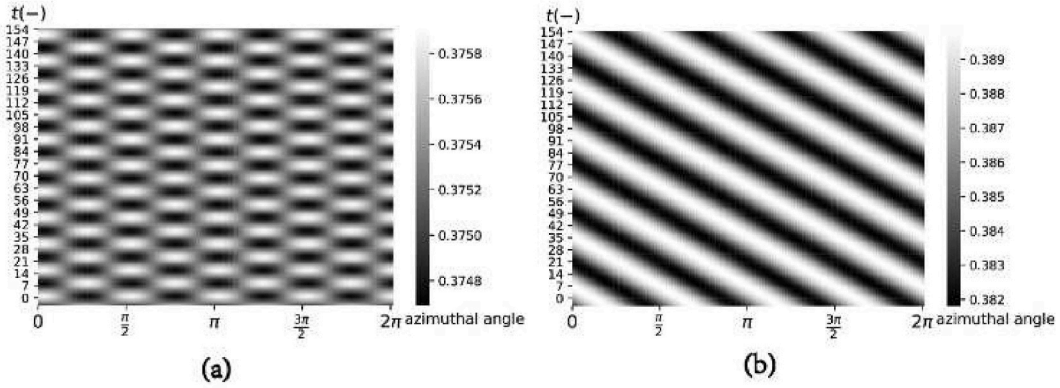

Fig. 4. Spatio-temporal diagram (STD) of the surface temperature along the azimuthal direction at $r = 12.0$ mm for $Vr = 0.809$. (a) At the critical stage ($\Delta T = 12.95$ K). (b) At slightly supercritical stage ($\Delta T = 13.40$ K).

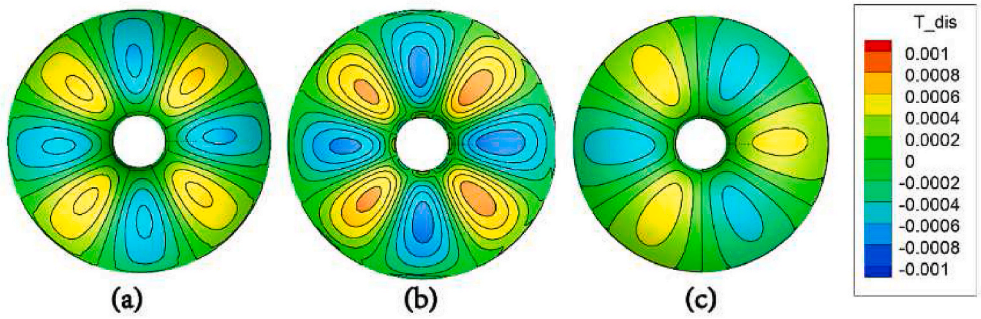

Fig. 5. Thermal disturbance field projections on the free surface at a certain moment at the critical stage for (a) $Vr = 0.809$, $\Delta T = 12.95$ K, $m = 4$, (b) $Vr = 1.113$, $\Delta T = 6.80$ K, $m = 4$, (c) $Vr = 1.173$, $\Delta T = 6.10$ K, $m = 3$.

disturbances ($T_{(HTW)}$) can be drawn by subtracting the pseudo steady axisymmetric temperature field (averaged over a few periods) from the instantaneous local temperature. Fig. 5 shows the temperature distributions on the free surface for $Vr = 0.809$, 1.113 and 1.173 at the critical conditions. Each pattern is composed of $2m$ (m brighter and m darker) polygons. These standing oscillations occur by superimposition of two hydrothermal waves traveling in opposite azimuthal directions.

Next two figures show snapshots of temperature disturbances in a vertical cut-plane near the antinode (Fig. 6) and the node (Fig. 7) of the standing wave (for $Vr = 0.809$, $\Delta T = 12.95$ K and $m = 4$) taken at the same instances during one period. It should be noted that the largest amplitude of the temperature oscillation appears near the bottom of the pool and the amplitude near the surface is much smaller. The amplitude of the temperature disturbance in Fig. 7 is much smaller than that in Fig. 6 because the cut plane in Fig. 7 locates near the nodes. Since the temperature disturbances shown in these two figures oscillate synchronously, the temperature disturbance in the critical stage indicates standing oscillation. The disturbance patterns for other Vr values show similar behaviors.

Note that the Fourier analysis of the surface temperature oscillation

Table 2
Critical and slightly supercritical conditions for pools with 8 liquid volume-ratios.

Vr	DNS-critical			DNS-slightly supercritica		
	ΔT_c/K	f_c/Hz	m_c	ΔT^*/K	f^*/Hz	m^*
0.809	12.92	0.0464	4	13.40	0.0478	4
0.855	11.72	0.0418	4	12.20	0.0437	4
0.905	10.32	0.0356	4	11.00	0.0403	4
0.940	9.52	0.0372	4	10.00	0.0383	4
1.000	8.33	0.0303	4	8.75	0.0355	4
1.045	7.67	0.0335	4	8.00	0.0340	4
1.113	6.75	0.0324	4	7.00	0.0327	4
1.173	6.05	0.0339	3	6.50	0.0337	3

in the critical stage for $Vr \leq 1.045$ show only one peak at the fundamental frequency (and its subharmonics, if any). On the other hand, the temperature oscillations for much fatter pools ($Vr = 1.113$ and 1.173) show two peaks, i.e. one higher peak at the fundamental frequency and a lower peak at frequencies very close to the fundamental frequency, as shown in Fig. 8. The Fourier analysis gives the frequencies for $Vr = 1.113$ as $f_1 = 0.0322$ Hz (fundamental frequency) and $f_2 = 0.0358$ Hz, and $f_1 = 0.0338$ Hz (fundamental frequency), $f_2 = 0.0315$ Hz for $Vr = 1.173$. The Dynamic Mode Decomposition (DMD) [46] is applied to investigate the inherent spatio-temporal evolution of the temperature oscillations. DMDs with ranks from 3 to 15 are tested to seek the optimal reduced-rank. The relative error between the reconstructed and the original data decreases from around 5%–2.5% by increasing the rank from 3 to 8, and the error retains 2.5% for ranks from 8 to 15. Therefore, number of DMD modes are set to be 8 for both *Vr*, and ordered by the magnitude of the amplitude coefficient of the initial snapshot. Fig. 9 shows the time evolution of the amplitude of each DMD modes for $Vr = 1.113$ under temperature difference near ΔT_c (≈6.80 K). Fig. 10 shows the spectral diagram of the time evolution of the seclected DMD modes and the corresponding temperature disturbances on the free surface. Mode 1 (first and second conjugated modes) has wavenumber $m = 4$ and $f_1 = 0.0319$ Hz, mode 2 (third and fourth conjugated modes) has $m = 8$ and $f_2 = 0.0655$ Hz, the fifth and sixth conjugated modes are non-oscillatory modes, and mode 3 (seventh and eighth conjugated modes) has $m = 3$ and $f_3 = 0.0351$ Hz.

For $Vr = 1.173$, the typical frequencies are $f_1 = 0.0338$ Hz, $f_2 = 0.0315$ Hz and $f_3 = 0.0680$ Hz as shown in Fig. 11, the first two conjugated modes are of $m = 3$ with frequency $f_1 = 0.0341$ Hz, the third and fourth are of $m = 4$ with frequency $f_2 = 0.0316$ Hz, the sixth and seventh are of $m = 6$ with frequency $f_3 = 0.0682$ Hz, the rest are non-oscillatory basic modes. Frequencies of the DMD modes are consistent with frequencies of the original thermal filed oscillation, thus it can be referred that two competitive wave modes with different wavenumbers(m) coexist during the development of the hydrothermal wave, and the dominating one overwhelms the other due to its larger amplitude

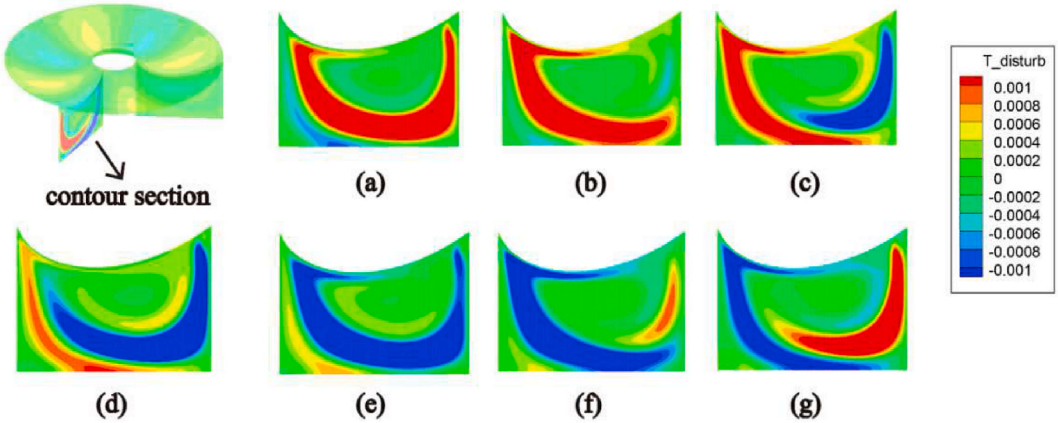

Fig. 6. Snapshots (a)–(g) during one period of thermal disturbance in a vertical cut near the antinode of the standing wave under critical condition $Vr = 0.809$, $\Delta T = 12.95$ K.

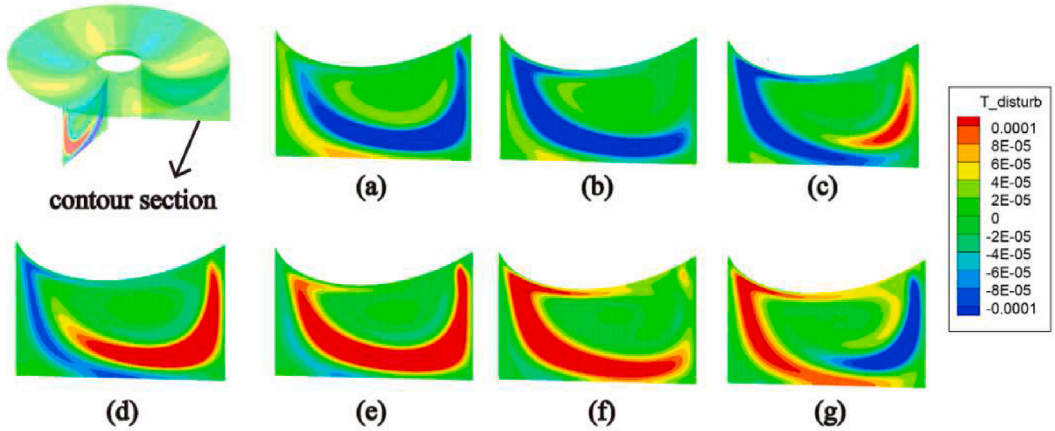

Fig. 7. Snapshots (a)–(g) during one period of longitudinal thermal disturbance projections near the node of the standing wave under critical condition $Vr = 0.809$, $\Delta T = 12.95$ K.

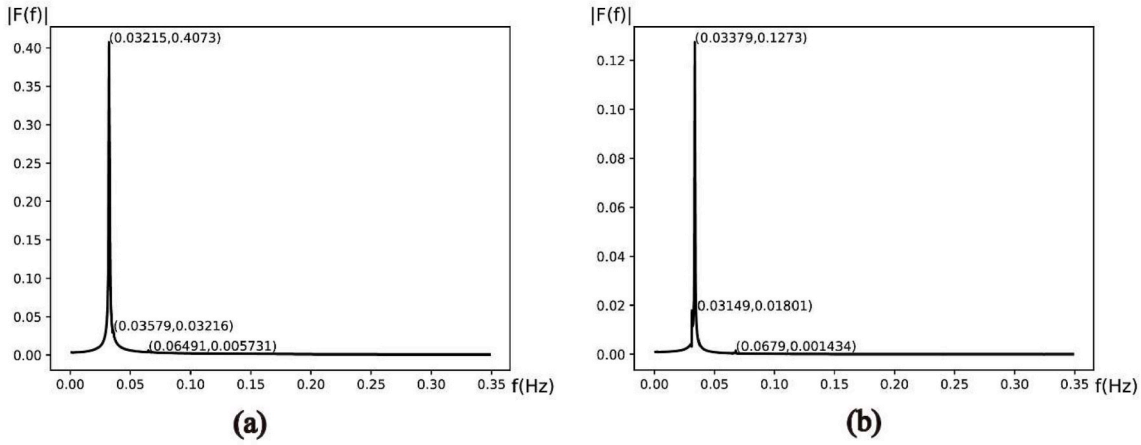

Fig. 8. Spectral diagram of temperature beneath the free surface for (a) $Vr = 1.113$, $\Delta T = 6.80$ K, (b) $Vr = 1.173$, $\Delta T = 6.10$ K

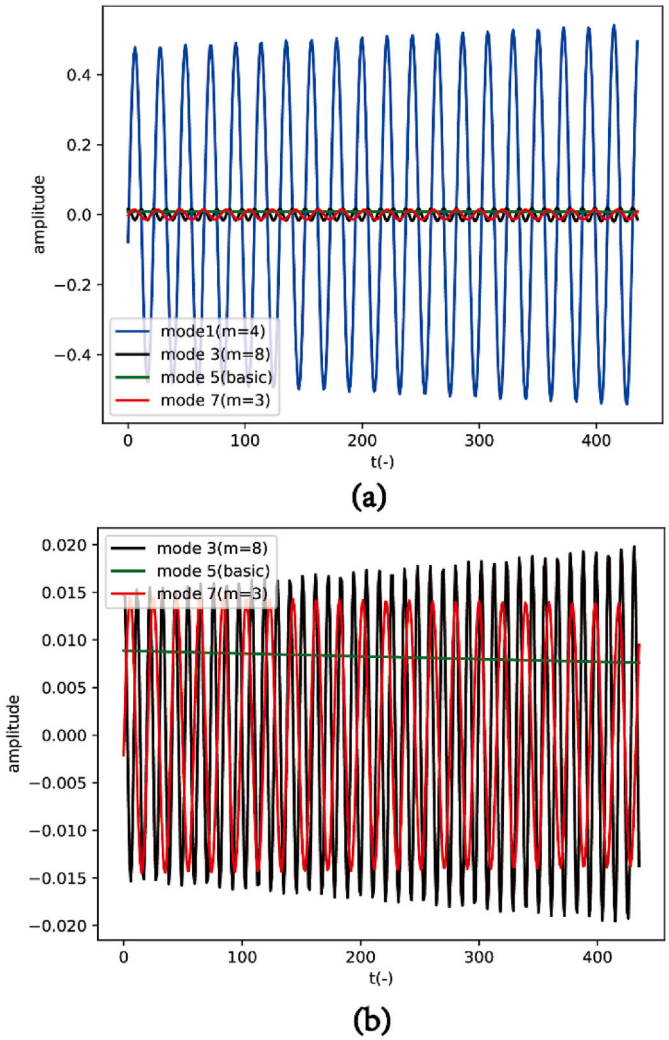

Fig. 9. Time evolution of amplitude coefficients of the DMD modes for $Vr = 1.113$, $\Delta T = 6.80$ K. (a) mode 1, mode3, mode 5 and mode7 (b) details of mode 3, mode 5, and mode 7.

contribution. For $Vr = 1.113$ and 1.173, the hydrothermal wavenumber is 4 and 3 respectively, which implies that the final mode selection of hydrothermal wave is apparently sensitive to the volume ratios.

3.4. *Traveling oscillatory flows*

As shown in Table 2, when the applied ΔT is slightly above the critical value, i.e., at the slightly supercritical stage with (ΔT^*, m^* and f^*), the oscillation frequency increases. Fig. 12 shows the temperature disturbance on the free surface at a certain moment at the slightly supercritical stage for $Vr = 0.809$, 1.113 and 1.173. It can be seen that the wavenumber remains unchanged compared to that at the critical stage. However, the motion of hydrothermal waves is sensitive to the applied temperature difference. Standing wave loses its stability and turns into traveling wave at the slightly supercritical stage, e.g., see Fig. 4b. Note that the m-wave structure is rotating along the azimuthal direction instead of pulsating locally.

4. Comparison with SJ-10 space experimental results

As mentioned above, a series of space experiments in an annular liquid pool were conducted on board the China's SJ-10 recovery satellite [15–17]. The free surface shape dependent instability of TC in microgravity was investigated. In the present study, the triple-phase-lines are supposed to be anchored at the top edge of the heating column and the outer wall as shown in Fig. 2. However, in the SJ-10 space experiments, the separation of the return capsule from the satellite causes a very large residual acceleration on the experimental apparatus. Unavoidably, some liquid escapes from the pool and some liquid attached on the wedge of the heating column, and the wedge lost the pinning power [17]. Thus the free surface shapes are different from those in the present study, especially for $Vr > 1.000$.

Table 3 compares the volume-ratio dependent critical conditions (ΔT_c, m_c and f_c) determined by the DNS (DNS-critical) and the SJ-10 space experiment (EXP) in the range of $0.809 \leq Vr \leq 1.000$. ΔT_c and f_c of the DNS show qualitatively similar Vr dependences as those of SJ-10 space experimental results except for some differences in quantity. The number of azimuthal waves (m) of the present DNS results is also generally same as those of SJ-10 experimental results. Possible major sources of the quantitative differences are discussed in the following paragraphs.

The present DNS assumes an adiabatic liquid surface but there exists heat exchanges between the ambient gas and the liquid surface. Sim

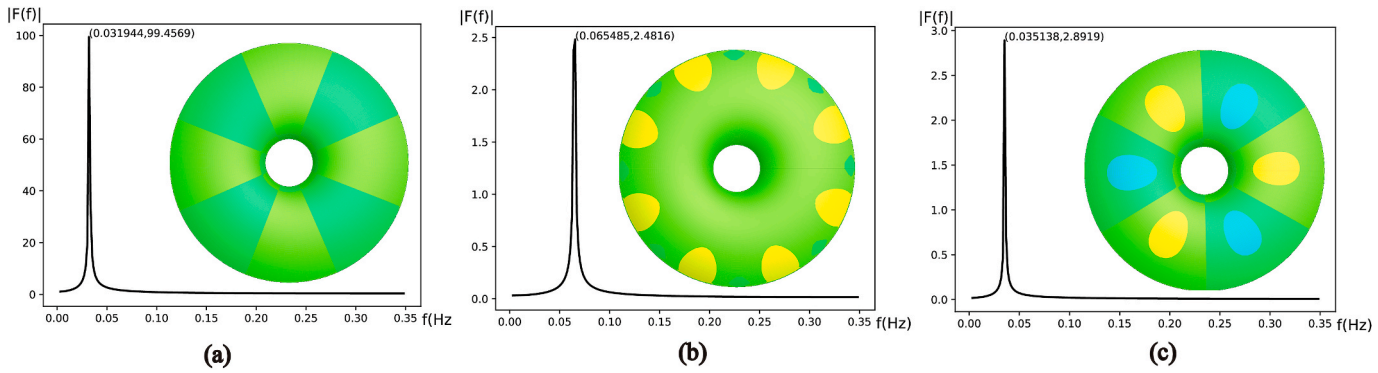

Fig. 10. Spectral diagram of the dynamics of the DMD modes and their temperature disturbance fields on the free surface for $Vr = 1.113$ $\Delta T = 6.80$ K (a) mode 1($m = 4$), (b) mode 3($m = 8$), (c) mode 7($m = 3$).

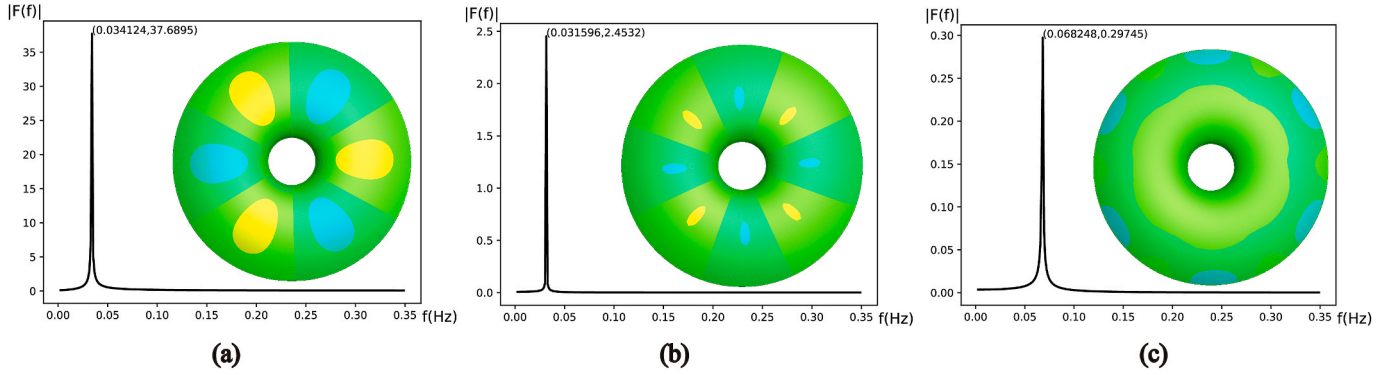

Fig. 11. Spectral diagram of the dynamics of the DMD modes and their temperature disturbance fields on the free surface for $Vr = 1.173$ $\Delta T = 6.10$ K (a) mode 1($m = 3$) (b) mode 3($m = 4$), (c) mode 6($m = 6$).

et al. [25,26] reported the significant effects of the interfacial heat transfer on the critical condition of thermocapillary flow in annular pools. In the SJ-10 space experiment payload, the ambient temperature was maintained at $T_{amb} = 291$ K which is slightly higher than the temperature of the outer wall (290 K). On the other hand, the surface of the solid central pole is higher than the liquid surface. Part of the heated gas around the central pole is driven by the liquid flow on the surface, then flows along the liquid surface toward the outer wall, and is mixed with the colder gas near the outer wall, thus there exists a weak return flow toward the central pole. The temperature distribution in the gas phase is not uniform but three dimensional. Accordingly, the direction of the heat flux through the liquid surface may change with the radial position. These temperature distributions are only given by a numerical simulation based on a set of fundamental equations and boundary conditions for liquid and gas phases. Such kind of simulation needs larger computer loads.

Here, in order to roughly assess the impact of the heat transfer through the liquid surface on the critical conditions, the boundary conditions on the liquid surface is replaced by Eq. (6). The last equation in Eq. (6) indicates that the heat exchange rate between the liquid surface and the ambient gas is kept at a temperature θ_A.

where $Bi = hd/\lambda$ and Θ_A=(T_{amb}-T_o)/ΔT is the Biot number and the non-dimensional ambient temperature, h is the heat transfer coefficient, and T_{amb} the ambient temperature. The simulation code is run for $Vr = 1.000$ and $T_{amb} = 291$ K. In this case, the liquid surface with local temperature higher than $T_{amb} = 291$ K is cooled. Since we do not know the correct value of h in the SJ-10 space experiment, DNS was run for $h = 0.5$ and 15.0 W/(m^{2}K) and the results are shown in Table 4.

These results show that the heat exchange through the interface stabilizes the basic flow and significantly increases ΔT_c. To simulate the phenomena correctly, information on the gas temperature and value of h must be given. However, there is no way to correctly estimate the gas temperature and h in the experimental equipment. For acurate and reliable critical condition, the velocity and temperature fields in the liquid and gas phases connected at the interphase must be solved together. (In some case, radiative heat transfer between the liquid surface and the surrounding solid walls must be considered even the temperature is not so high.)

Detailed LSA code and new simulation code, which consider the heat transfer through the interface, are developing. Systematic results will be reported elsewhere.

$$\vec{t}_{\xi_1} \cdot \prod \vec{n} = Ma \nabla \Theta \cdot \vec{t}_{\xi_1}, \quad \vec{t}_{\xi_2} \cdot \prod \vec{n} = Ma \nabla \Theta \cdot \vec{t}_{\xi_2}, \quad \vec{U} \cdot \vec{n} = 0, \nabla \Theta \cdot \vec{n} = Bi(\Theta - \Theta_A) \tag{6}$$

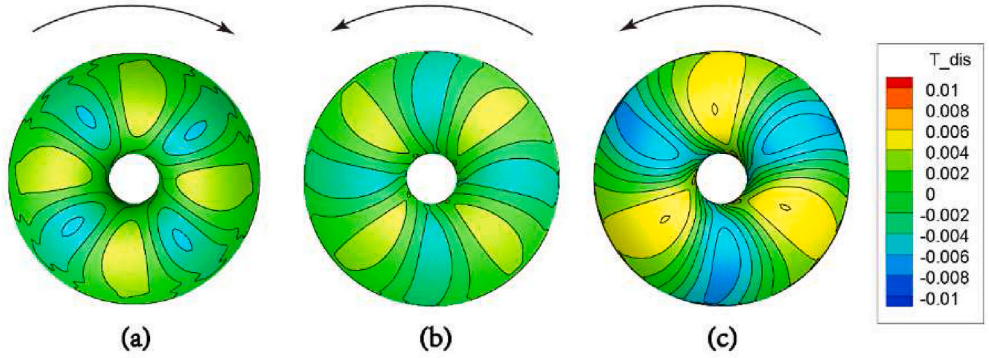

Fig. 12. Temperature disturbance on the free surface at a certain moment at the slightly supercritical stage: (a) $Vr = 0.809$, $\Delta T = 13.40$ K, $m = 4$ (clockwise), (b) $Vr = 1.113$, $\Delta T = 7.00$ K, $m = 4$ (counter-clockwise), (c) $Vr = 1.173$, $\Delta T = 6.50$ K, $m = 3$ (counter-clockwise).

Table 3
Comparison of critical conditions determined by the DNS (DNS-critical) and the SJ-10 space experiment (EXP) for $0.809 \leq \mathrm{Vr} \leq 1.000$.

Vr	EXP			DNS-critical		
	ΔT_c/K	f_c/Hz	m_c	ΔT_c/K	f_c/Hz	m_c
0.809	18.26	0.0525	3	12.92	0.0464	4
0.855	19.35	0.0525	4	11.72	0.0418	4
0.905	16.80	0.0525	4	10.32	0.0356	4
0.940	14.04	0.0450	4	9.52	0.0372	4
1.000	14.95	0.0450	4	8.33	0.0303	4

Table 4
DNS results about the effect of h (heat transfer coefficient) on the ΔT_c for the present liquid pool with $Vr = 1.000$.

Vr	h W/(m^{2}K)	T_{amb}/K	ΔT_c/K	f_c/Hz	m_c
1.000	Exp	291	14.95	0.0450	4
	0.0	291	8.33	0.0303	4
	0.5	291	8.60	0.0380	4
	15.0	291	14.85	0.0540	4
0.809	Exp	291	18.26	0.0525	3
	0.0	291	12.92	0.0464	4
	15.0	291	23.50	0.0871	4

5. Conclusion

In the present study, direct numerical simulations, assuming adiabatic boundary condition at the liquid surface, are adopted to investigate the thermocapillary convection in annular liquid pools with different liquid volume ratios ($0.809 \leq Vr \leq 1.173$). Numerical simulations reveal that the volume ratios have significant effects on the critical condition for the onset of oscillatory thermocapillary convection. The critical temperature difference ΔT_c and the corresponding oscillation frequency f_c decrease with the increasing volume ratios *Vr*. At the critical stage, the TC is the standing oscillation with wavenumber $m = 4$ for all volume ratios studied except $m = 3$ for the case $Vr = 1.173$. The standing oscillation is rather unstable and is replaced by the traveling oscillation having the same wave number at the slightly supercritical stage.

The critical conditions predicted by the present numerical simulation show qualitatively similar *Vr* dependencies of the results of the SJ-10 space experiments for small *Vr*. However, the calculated ΔT_c is much smaller than the results of the space experiments. Slightly modified numerical code, in which the boundary condition at the liquid surface is replaced by a convective heat transfer condition between the liquid surface and the gas at which the temperautre T is assumed to be 291 K, predicts significant stabilization of the basic flow for $h = 15$ [W/m K]. However, the reliable h value and the gas temperature in the space experiment are not known. Results of numerical simulations calculated by a new code, which calculate the velocity and temperature fields combined by boundary conditions at the interface, will be reported elsewhere.

Declaration of competing interest

The authors declare that they have no known competing financial interests or personal relationships that could have appeared to influence the work reported in this paper.

Data availability

Data will be made available on request.

Acknowledgement

This work was supported by the National Natural Science Foundation of China (Grant No. 11972353,12172363 and 12032020).

References

[1] S.H. Davis, Thermocapillary instabilities, Annu. Rev. Fluid Mech. 19 (1987) 403–435, https://doi.org/10.1146/annurev.fl.19.010187.002155.
[2] M.F. Schatz, G.P. Neitzel, Experiments on thermocapillary instabilities, Annu. Rev. Fluid Mech. 33 (2001) 93–127.
[3] W.R. Hu, Z.M. Tang, K. Li, Thermocapillary convection in floating zones, Appl. Mech. Rev. 61 (2008).
[4] T. Azami, S. Nakamura, M. Eguchi, T. Hibiya, The role of surface-tension-driven flow in the formation of a surface pattern on a Czochralski silicon melt, J. Cryst. Growth 233 (2001) 99–107.
[5] V. Shevtsova, A. Nepomnyashchy, J.C. Legros, Thermocapillary-buoyancy convection in a shallow cavity heated from the side, Phys. Rev. E. 67 (2003), 066308.
[6] C.L. Chan, C. Chen, Effect of gravity on the stability of thermocapillary convection in a horizontal fluid layer, J. Fluid Mech. 647 (2010) 91–103.
[7] Y. Kamotani, A. Chang, S. Ostrach, Effects of Heating Mode on Steady Axisymmetric Thermocapillary Flows in Microgravity, 1996.
[8] Y. Kamotani, J. Lee, S. Ostrach, A. Pline, An experimental study of oscillatory thermocapillary convection in cylindrical containers, Phys. Fluids 4 (1992) 955–962.
[9] Y. Kamotani, S. Ostrach, A. Pline, A Thermocapillary Convection Experiment in Microgravity, 1995.
[10] Y. Kamotani, S. Ostrach, J. Masud, Oscillatory thermocapillary flows in open cylindrical containers induced by CO2 laser heating, Int. J. Heat Mass Tran. 42 (1999) 555–564.
[11] D. Schwabe, A. Cramer, J. Schneider, S. Benz, J. Metzger, Experiments on the multi-roll-structure of thermocapillary flow in side-heated thin liquid layers, Adv. Space Res. 24 (1999) 1367–1373.
[12] D. Schwabe, S. Benz, Thermocapillary flow instabilities in an annulus under microgravity—results of the experiment magia, Adv. Space Res. 29 (2002) 629–638.
[13] S.N. Aristov, K.G. Schwarz, Rotating influence on thermocapillary flow in zero-gravity state, Microgravity Sci. Technol. VIII (1995) 101–105.
[14] D. Villers, J.K. Platten, Coupled buoyancy and Marangoni convection in acetone: experiments and comparison with numerical simulations, J. Fluid Mech. 234 (1992) 487, https://doi.org/10.1017/S0022112092000880.

[15] Q. Kang, H. Jiang, L. Duan, C. Zhang, W. Hu, The critical condition and oscillation-transition characteristics of thermocapillary convection in the space experiment on SJ-10 satellite, Int. J. Heat Mass Tran. 135 (2019) 479–490.
[16] Q. Kang, J. Wang, L. Duan, Y. Su, J. He, D. Wu, W. Hu, The volume ratio effect on flow patterns and transition processes of thermocapillary convection, J. Fluid Mech. 868 (2019) 560–583.
[17] Q. Kang, D. Wu, L. Duan, J. He, L. Hu, L. Duan, W. Hu, Surface configurations and wave patterns of thermocapillary convection onboard the SJ10 satellite, Phys. Fluids 31 (2019), 044105.
[18] M. Smith, S. Davis, Instabilities of dynamic thermocapillary liquid layer. Part 2. Surface wave instability, J. Fluid Mech. 132 (1983) 132–144.
[19] M.K. Smith, S.H. Davis, Instabilities of dynamic thermocapillary liquid layers. Part 1. Convective instabilities, J. Fluid Mech. 132 (1983) 119–144.
[20] M.K. Smith, Instability mechanisms in dynamic thermocapillary liquid layers, Phys. Fluids 29 (1986) 3182–3186.
[21] C. Baiocci, V.V. Pukhnachev, Problems with one-sided constraints for Navier-Stokes equations and the dynamic contact angle, J. Appl. Mech. Tech. Phys. 31 (1990) 185–197, https://doi.org/10.1007/BF00851827.
[22] V.V. Pukhnachev, Interaction between a distributed source and the free surface of a viscous fluid, Fluid Dynam. 31 (1996) 206–217, https://doi.org/10.1007/BF02029679.
[23] K. Shvarts, A. Boudlal, Effect of rotation on stability of advective flow in horizontal liquid layer with a free upper boundary, J. Phys. Conf. 216 (2010), 012005, https://doi.org/10.1088/1742-6596/216/1/012005.
[24] N.S. Knutova, K.G. Shvarts, A study of behavior and stability of an advective thermocapillary flow in a weakly rotating liquid layer under microgravity, Fluid Dynam. 50 (2015) 340–350, https://doi.org/10.1134/S0015462815030047.
[25] B.-C. Sim, A. Zebib, Effect of free surface heat loss and rotation on transition to oscillatory thermocapillary convection, Phys. Fluids 14 (2002) 225–231.
[26] B.-C. Sim, A. Zebib, D. Schwabe, Oscillatory thermocapillary convection in open cylindrical annuli. Part 2. Simulations, J. Fluid Mech. 491 (2003) 259–274.
[27] C.-M. Wu, J.-H. Chen, B. Yuan, Y.-R. Li, Bifurcations and pattern evolutions of thermo-solutocapillary flow in rotating cylinder with a top disk, Phys. Fluids 31 (2019), 094103.
[28] O.A. Bessonov, V.I. Polezhaev, Unsteady nonaxisymmetric flows in the hydrodynamic Czochralski model at high Prandtl numbers, Fluid Dynam. 46 (2011) 684–698, https://doi.org/10.1134/S0015462811050024.
[29] O.A. Bessonov, V.I. Polezhaev, Instabilities of thermal gravitational convection and heat transfer in the Czochralski model at different Prandtl numbers, Fluid Dynam. 48 (2013) 23–35, https://doi.org/10.1134/S0015462813010043.
[30] O.A. Bessonov, V.I. Polezhaev, Regime diagram and three-dimensional effects of convective interactions in the hydrodynamic Czochralski model, Fluid Dynam. 49 (2014) 149–159, https://doi.org/10.1134/S0015462814020045.
[31] V.B. Bekezhanova, O.N. Goncharova, Three-dimensional thermocapillary flow regimes with evaporation, J. Phys. Conf. 894 (2017), 012023, https://doi.org/10.1088/1742-6596/894/1/012023.
[32] V.B. Bekezhanova, O.N. Goncharova, Thermocapillary convection with phase transition in the 3D channel in a weak gravity field, Microgravity Sci. Technol. 31 (2019) 357–376, https://doi.org/10.1007/s12217-019-9691-4.
[33] V.B. Bekezhanova, O.N. Goncharova, Modeling of three dimensional thermocapillary flows with evaporation at the interface based on the solutions of a special type of the convection equations, Appl. Math. Model. 62 (2018) 145–162, https://doi.org/10.1016/j.apm.2018.05.021.
[34] V.B. Bekezhanova, O.N. Goncharova, Thermodiffusion effects in a two-phase system with the thermocapillary deformable interface exposed to local heating, Int. J. Multiphas. Flow 152 (2022) 104080, https://doi.org/10.1016/j.ijmultiphaseflow.2022.104080.
[35] W. Shi, N. Imaishi, Hydrothermal waves in differentially heated shallow annular pools of silicone oil, J. Cryst. Growth 290 (2006) 280–291.
[36] S. Hoyas, H. Herrero, A. Mancho, Bifurcation diversity of dynamic thermocapillary liquid layers, Phys. Rev. E. 66 (2002), 057301.
[37] C. Jing, T. Tsukada, M. Hozawa, K. Shimamura, N. Ichinose, T. Shishido, Numerical studies of wave pattern in an oxide melt in the Czochralski crystal growth, J. Cryst. Growth 265 (2004) 505–517.
[38] B. Basu, S. Enger, M. Breuer, F. Durst, Three-dimensional simulation of flow and thermal field in a Czochralski melt using a block-structured finite-volume method, J. Cryst. Growth 219 (2000) 123–143, https://doi.org/10.1016/S0022-0248(00)00591-1.
[39] S. Sankaranarayanan, M.L. Spaulding, Dispersion and stability analyses of the linearized two-dimensional shallow water equations in boundary-fitted co-ordinates, Int. J. Numer. Methods Fluid. 42 (2003) 741–763.
[40] K. Badcock, B. Richards, M. Woodgate, Elements of computational fluid dynamics on block structured grids using implicit solvers, Prog. Aero. Sci. 36 (2000) 351–392.
[41] C. Rhie, W.L. Chow, Numerical study of the turbulent flow past an airfoil with trailing edge separation, AIAA J. 21 (1983) 1525–1532.
[42] B. Leonard, The QUICK algorithm-A uniformly third-order finite-difference method for highly convective flows, Comput. Methods Fluids (1980) 159–195.
[43] S.V. Patankar, Numerical Heat Transfer and Fluid Flow, Hemisphere Publishing Corp., Washington, DC, 1980.
[44] C. Jing, S. Ihara, K.-I. Sugioka, T. Tsukada, M. Kobayashi, Global analysis of heat transfer in CZ crystal growth of oxide taking into account three-dimensional unsteady melt convection: effect of meniscus shape, J. Cryst. Growth 310 (2008) 204–213.
[45] H. Liu, Z. Zeng, L. Yin, Z. Qiu, L. Qiao, Volume effect on the instabilities of thermocapillary flow in annular pools filled with silicon melt, Int. Commun. Heat Mass Tran. 121 (2021) 105099, https://doi.org/10.1016/j.icheatmasstransfer.2020.105099.
[46] N. Demo, M. Tezzele, G. Rozza, PyDMD: Python dynamic mode decomposition, JOSS 3 (2018) 530, https://doi.org/10.21105/joss.00530.